

論文 / 著書情報
Article / Book Information

Title	Particle-in-cell simulation of magnetic-assisted electrostatic confinement device
Author	Kunihiko Tomiyasu, Kai Yokoyama, Masato Watanabe, Eiki Hotta
Journal/Book name	Fusion Engineering and Design, Vol. 85, , pp. 728-733
Issue date	2010, 8
URL	http://www.journals.elsevier.com/fusion-engineering-and-design
DOI	http://dx.doi.org/10.1016/j.fusengdes.2010.04.036
Note	このファイルは著者（最終）版です。 This file is author (final) version

Particle-in-cell simulation of magnetic-assisted electrostatic confinement device

Kunihiko Tomiyasu*, Kai Yokoyama, Masato Watanabe, and Eiki Hotta

*Department of Energy Sciences, Tokyo Institute of Technology,
4259 Nagatsuta, Midori-ku, Yokohama 226-8502, Japan*

Abstract

In order to enhance the fusion reaction rate in Inertial Electrostatic Confinement devices, it is necessary to increase the ion density with low cathode current and low background pressure. In order to accomplish the requirement, the authors suggest Magnetic-assisted Electrostatic Confinement (MEC) scheme. The MEC relies on controlling the ion motion by applying an axial magnetic field to a system with cylindrical electrodes. In order to clarify the fundamental performances of the MEC device, Particle-in-Cell simulation was carried out. By reducing the background pressure, the ion confinement was improved resulting in the increase of the ion density. However, the ion density saturated due to space charge limitation. The estimated fusion reaction rate was about 5×10^6 1/s/m when the cathode voltage was -100 kV, the magnetic field was 200 mT, and the cathode current was 100 mA/m. The reaction rate, however, is expected to become higher since the ion density limitation is moderated by the electron which is not considered in the present analysis.

Keywords: Inertial electrostatic confinement, Fusion, Particle in cell

*Corresponding author

E-mail: tomiyasu.k.aa@m.titech.ac.jp

Postal address: 4259 Nagatsuta, Midori-ku, Yokohama 226-8502, Japan

Telephone: +81-45-924-5698

Fax: +81-45-924-5697

1. Introduction

A concept to confine ions electrostatically in a spherical or cylindrical geometry is called Inertial Electrostatic Confinement (IEC) [1]. Ions are accelerated to fusion-relevant energies by the electric field between concentric electrodes and circulate inside the outer anode through the inner gridded cathode. Since the IEC device has several features, such as simple configuration, compact size, and high controllability, the fusion device is expected to be used as a portable neutron/proton source [2-4]. However, substantial enhancement of the neutron yield is necessary for practical applications. For instance, cancer therapy called Boron Neutron Capture Therapy requires at least 10^9 n/cm²/s of neutron flux [5]. On the other hand, achieved neutron yield with the IEC device in steady state is about 10^8 n/s which corresponds to a neutron flux of about 10^4 n/cm²/s at the surface of the device [6].

In order to improve the fusion reaction rate, following two ways have been investigated by several research groups. One is to increase the ion density by increasing the input current [2,7,8]. The other is to increase the ion energy by reducing the background gas pressure which reduces the energy loss due to collisions with background neutrals [9-12]. As the input current is increased, however, electrode melting is expected. As the pressure is reduced, it becomes hard to increase the ion density. In order to accomplish the two requirements, both of the ion and the electron confinements need to be improved. Better ion confinement leads to higher ion density with lower input current. Better electron confinement leads to more ion production under lower background gas pressure.

Current IEC devices rely on a gridded electrode system. Hence, the possibility for the ions to pass through the cathode never exceeds a geometrical transparency of the cathode grid which is around 0.90 to 0.97 [6,12-14]. In order to see the relation between the cathode transparency and the ion density, a rough estimation is made as follows. In a cylindrical geometry, it is assumed that a space charge of the ion does not affect the electric potential, that is the potential between the cylindrical electrodes is a vacuum potential and the potential inside the cathode is flat as shown in Fig. 1. The energy of the ion at the anode is zero, and the ions do not collide with the other particles. When the probability for the ions to pass through the cathode is the geometrical cathode transparency, η , the ion density, n_i , is given by

$$n_i = \frac{I_i}{qv \cdot 2\pi rh} \quad (1)$$

$$\begin{aligned}
I_i &= \frac{2\eta}{1-\eta^2} I_c & (0 < r < r_c) \\
I_i &= \frac{1+\eta^2}{1-\eta^2} I_c & (r_c < r < r_a)
\end{aligned} \tag{2}$$

where I_i is sum of the inward and outward ion current as shown in Fig. 1, q and v are charge and velocity of the ion, r is radial position, h is height of the electrode, I_c is cathode current, and r_c and r_a are radii of the cathode and the anode. From the energy conservation, the ion velocity is given by a function of radius. Figure 2 shows the ion density distribution with several cathode transparencies when the radii of the cathode and the anode are 10 mm and 100 mm, the cathode current and voltage are 1 A/m and -100 kV, and the anode is grounded. Note that the estimated result inside the cathode does not have enough reliability since the potential inside the cathode is not expected to be flat due to the ion space charge, and the ions cannot reach to the center due to the conservation of the angular momentum. Hence the estimated result inside the cathode is excluded. When the cathode transparency is 0.9, the ion density is in the order of 10^{14} m^{-3} . When the cathode transparency is improved to 0.99 or 0.999, the ion density increases to the order of 10^{15} or 10^{16} m^{-3} .

As a feasible approach to improve the ion and the electron confinements, the authors suggest Magnetic-assisted Electrostatic Confinement (MEC) device. In the present study, a numerical simulation was carried out by using a Particle-in-Cell (PIC) simulation with Monte Carlo collision scheme [15]. Fundamental performances of the MEC device under several operating conditions are reported.

2. Magnetic-assisted electrostatic confinement

A schematic of the MEC device is shown in Fig. 3. An axial magnetic field is applied to a system with cylindrical electrodes. The ions are forced to an azimuthal direction by Lorentz force as well as they are accelerated toward the center by the electric field. Hence, the ion motion can be controlled by applying an appropriate magnetic field so that the ion can avoid colliding with the cathode.

An ideal motion of a deuterium molecular ion is shown in Fig. 4. The ion circulates inside the device and is completely confined if there is no interaction with the other particles. Hence, it is naturally expected that the ion confinement is improved as the background pressure is reduced. The required magnetic field for the ion to avoid colliding with the cathode can be analytically derived from the conservation of the energy, W , and the canonical angular momentum, p_θ ,

$$W = \frac{1}{2}m(v_r^2 + v_\theta^2) + q\phi \quad (3)$$

$$p_\theta = r(mv_\theta + qA_\theta) \quad (4)$$

where m , v , and q are mass, velocity, and charge of the ion, ϕ is electric potential, r is radial position, A is vector potential, and the subscript r or θ represents radial or angular component. In a cylindrically symmetric geometry, the angular component of the vector potential is given by

$$A_\theta = \frac{B_z r}{2} - \frac{1}{2r} \quad (5)$$

where B_z is applied axial magnetic field. In order to avoid colliding with the cathode, the radial velocity of the ion must be zero at a radial position larger than the cathode radius. Assuming that the ion is produced near the anode with zero energy and the ion does not collide with the background neutrals, the required magnetic field, B_{req} , is given by

$$B_{req} = \frac{2r_c}{r_a^2 - r_c^2} \sqrt{\frac{2m(\phi_a - \phi_c)}{q}} \quad (6)$$

where r is radius, ϕ electric potential, and the subscript a or c represents anode or cathode. The required magnetic field at a different cathode voltage is shown in Fig. 5. The radii of the cathode and the anode are 10 mm and 100 mm, respectively. When the anode is grounded, the required magnetic field increases in proportion to square root of the cathode voltage. For instance, it ranges from 60 to 190 mT when the cathode voltage changes from -10 to -100 kV. The ion orbits under the magnetic field of 200, 300, and 400 mT are shown in Fig. 6 when the cathode voltage is -100 kV, the radii of the cathode and the anode are 10 mm and 100 mm. When the magnetic field is too strong, the ion orbit is largely distorted. It leads to that the ion does not obtain enough kinetic energy from the potential well since the ion cannot approach the cathode. Hence, the axial magnetic field should be adjusted at the required value as shown in Fig. 5 depending on the applying voltage.

In the MEC device, thermal electrons from the filament near the anode are intended to be used for the ion production. The electrons are trapped by the magnetic field and drift in the azimuthal direction. Hence, enough ion production due to electron impact ionization is expected even under the low background pressure. The electron confinement plays another roll in the MEC. That is a neutralization of the ion space charge between the electrodes. The ion density is limited by the space charge which is highly dependent on the electrode size and the applying voltage. However, it is expected that higher ion density can be achieved since the electrons are confined as well as the ions.

In the MEC device, the cathode shape can be simplified such as a general pipe while it is a gridded configuration in a conventional IEC device. Since water cooling of the cathode is easily made in the MEC device, the input current can be increased furthermore.

3. Numerical methods and models

One dimensional Poisson equation in a cylindrical geometry is solved by using a finite difference method,

$$\frac{1}{r} \frac{\partial \phi}{\partial r} + \frac{\partial^2 \phi}{\partial r^2} = -\frac{\rho}{\epsilon_0} \quad (7)$$

where ϕ is electric potential, ρ is charge density, and ϵ_0 is dielectric constant in a vacuum. Radial mesh size is about 1.0 mm. Then iterative calculations are made with Successive-Over-Relaxation method and multi-grid method where the convergence condition is $|\Delta\phi/\phi| < 10^{-7}$.

Equation of motion in a cylindrical geometry is solved by using Runge-Kutta method with fourth order of accuracy,

$$\begin{aligned} \frac{dv_r}{dt} &= \frac{q}{m} (E_r + v_\theta B_z) + \frac{1}{r} v_\theta^2 \\ \frac{dv_\theta}{dt} &= -\frac{q}{m} v_r B_z - \frac{1}{r} v_r v_\theta \\ \frac{dr}{dt} &= v_r \\ \frac{d\theta}{dt} &= \frac{1}{r} v_\theta \end{aligned} \quad (8)$$

where v , q , and m are velocity, charge, and mass of the particle, E is electric field, and B is magnetic field. The subscript r , θ , or z represents radial, angular, or axial component. Linear interpolations are used for the charge of the particle to the grids and the electric field at the spatial grids to the particle. Time step of the calculation is 100 ps. The particle motion is tracked in two dimensions, r - θ , while the electric potential is calculated in one dimension, r , assuming a symmetric distribution around z -axis. In the present calculation, only deuterium molecular ion is considered due to an enormous computational time for the electrons and a complexity of the interaction modeling between the ions and the electrons.

Collision processes between the ions and the background neutrals rely on Monte Carlo Collision scheme [15]. In the present calculation, elastic scattering, charge exchange reaction and ion impact

ionization are included. A fast neutral to be produced via charge exchange reaction and an electron to be produced via ion impact ionization are not considered. Cross sections of the reactions are referred from the published data [16].

Fusion reactions in the IEC device occur in many different modes which are among ion beams, fast neutrals, background neutrals, and embedded particles in the electrodes or the chamber wall. In the present calculation, the ion beam and the background neutral are considered. Accordingly, beam-background reaction rate, $R_{\text{BM-BG}}$, and beam-beam reaction rate, $R_{\text{BM-BM}}$, are estimated,

$$R_{\text{BM-BG}} = \int_V n_i n_{\text{gas}} \langle \sigma v \rangle dV \quad (9)$$

$$R_{\text{BM-BM}} = \int_V \left(\frac{n_i}{2} \right)^2 \langle \sigma v \rangle dV \quad (10)$$

where n_i is ion density, n_{gas} is background gas density, σ is D-D fusion cross section [17], v is relative velocity of the particles. In the beam-background reaction, v is the relative velocity between the background neutral and the incident ion. In the beam-beam reaction, v is assumed to be the double of the radial velocity of the ion since the radial velocities of the inward and outward ions at a certain radius are positive and negative with same magnitude and the azimuthal velocities are same in the ideal motion. The cross section, σ , at the energy corresponding to the relative velocity is used. During the estimation of the fusion reaction, super particles are not lost since the reaction rate is much smaller than the weight of the super particle divided by the calculation time step.

Numerical models are based on a typical IEC device and its operational condition. The radii of the cathode and the anode are 10 mm and 100 mm. Parametric study is carried out by changing the background pressure from 1 to 100 mPa, the cathode current from 1 to 100 mA/m, the cathode voltage from -10 to -100 kV, and the axial magnetic field from 100 to 400 mT. Deuterium molecular ions are produced near the anode with no initial energy as an input. The input ion current is controlled so that the cathode current becomes a selected value. A contribution of the secondary electron is not included since the electron is expected to hit the cathode again after the Larmor motion. Calculation is continued until it reaches steady state in terms of the cathode current, the number of the super particle, and so on. Weight of the super particle is controlled so that the number of the super particle stays within a selected range.

4. Results and discussions

4.1 Effective cathode transparency

In order to evaluate the effective cathode transparency in the MEC system, preliminary calculations were carried out. The averaged lifetime was computed by tracking 1,000 ions which was produced near the anode with zero energy. The radii of the cathode and the anode were 10 mm and 100 mm, the cathode voltage was -100 kV, and the axial magnetic field was 200 mT. Figure 7 shows the averaged lifetime of the ion and the corresponding effective cathode transparency at a background pressure from 1 to 100 mPa. The effective cathode transparency, η , is calculated by

$$\eta = 1 - \frac{T}{t} \quad (9)$$

where t is the averaged lifetime of the ion, and T is the time for the ion to reach the center from the anode when the cathode transparency is 1.0 without any collisions and any axial magnetic field. For the present device size and the applying voltage, T is about 124 ns. The lifetime increased as the background pressure was reduced. The effective cathode transparency at the background pressure of 1, 10, and 100 mPa were 0.999, 0.993, and 0.936.

4.2 Dependence on background pressure

The ion density and the potential distribution at the pressure of 1, 10, or 100 mPa are shown in Fig. 8. Cathode voltage, cathode current, and magnetic field are -100 kV, 100 mA/m, and 200 mT. As far as the cathode current at the pressure of 1 mPa is concerned, it did not reach 100 mA/m due to space charge limitation. As the pressure was reduced by one order, the ion density increased by approximately one order. It indicates that the ion confinement is improved by reducing the pressure. However, the ion density saturated around 10^{15} m^{-3} due to space charge limitation. The space charge limitation can be seen in the potential distribution in Fig. 8 (b). The potential near the anode is flat at the pressure of 1 mPa indicating that no more additional ions can enter the potential well. The potential distribution at the pressure of 100 mPa was almost the same as the vacuum potential.

Energy distributions of the ion at the pressure of 1, 10, and 100 mPa are shown in Fig. 9. All parameters are the same as those in Fig. 8. It is seen that the upper edge of the energy distribution corresponds to the potential profile. As the pressure is reduced, the ion confinement is improved and the ion density increases. As the ion space charge approaches the limitation, structure of the potential well becomes steep and narrow. It is also seen that a dispersion of the ion energy becomes large as the pressure is increased. This is because the collision frequency between the ions and the background neutrals increases. The difference of the energy dispersion indicates that more effective acceleration of

the ion is achieved at lower background pressure.

Dependence of the fusion reaction rate on the background pressure is shown in Fig. 10. Cathode current of 1, 10, and 100 mA/m was investigated. All the other parameters are the same as those in Fig. 8. Beam-background reaction (BM-BG) was dominant in the present pressure range, which is from 1 to 100 mPa, since the ion density saturated around 10^{15} m^{-3} while the background neutral density ranged from 10^{17} to 10^{20} m^{-3} . Beam-background reaction rate was almost the same at a different pressure. The main reason is that the ion density decreases almost in inverse proportion to the pressure as shown in Fig. 8 while the neutral density increases in proportion to the pressure. Since beam-background reaction rate is proportional to the product of the ion density and the neutral density, the reaction rate does not change even when the background pressure is different in the MEC. As the pressure is reduced, beam-beam reaction rate increased in inverse proportion to the square of the pressure. This is because the reaction rate is proportional to the square of the ion density which increases almost in inverse proportion to the pressure.

4.3 Dependence on magnetic field

The ion density distribution under the magnetic field of 100, 200, 300, or 400 mT is shown in Fig. 11. Cathode voltage, cathode current, and background pressure are -100 kV , 100 mA/m , and 10 mPa . When the magnetic field exceeded 190 mT , which was the required value under the vacuum potential, the ion density increased by an order of approximately two. Then the peak of the density shifted outward as the magnetic field increases as expected in Fig. 6. Hence the required magnetic field under the vacuum potential is regarded to be an optimum value even when the space charge is reflected to the potential profile.

Dependence of the fusion reaction rate on the background pressure is shown in Fig. 12. All parameters are the same as those in Fig. 11. Once the magnetic field exceeded the required value, beam-background reaction increased by an order of approximately two since it is proportional to the ion density. Similarly, beam-beam reaction increased by an order of approximately four as the magnetic field exceeded the required value since the reaction rate is proportional to the square of the ion density. As the magnetic field increased afterward, both reaction rates gradually decreased. When the magnetic field is too strong, the ion cannot get close to the cathode as shown in Figs. 6 and 11. That means the ions cannot obtain full energy from the electric potential. That is why the reaction rates decreased gradually.

The estimated total fusion reaction rate was $5 \times 10^6 \text{ 1/s/m}$ under the present operating conditions.

The present calculation, however, the electron is not considered. Since the electrons are also confined in the system, it is expected that a certain amount of the ion charge is neutralized. Since it leads to moderating the ion space charge limitation, more reaction rate is expected in a practical device. In order to increase the fusion reaction rate, it is required to moderate the space charge limitation. The allowable space charge increases as the applying voltage is increased, the anode is narrowed, and the cathode becomes wide [18]. By optimizing the size of the electrodes depending on the achievable applying voltage and magnetic field, the highest fusion reaction rate is expected to be achieved.

5. Conclusions

In order to obtain high ion density with low cathode current and low background pressure in the IEC fusion device, the authors suggest Magnetic-assisted Electrostatic Confinement scheme. As a result of a preliminary PIC simulation, fundamental performances of the MEC device were clarified. By reducing the background pressure, the ion confinement improved. The effective cathode transparency at the background pressure of 1, 10, and 100 mPa were 0.999, 0.993, and 0.936. As the pressure was reduced by one order, the ion density increased by approximately one order with a constant cathode current. However, the ion density saturated due to space charge limitation. It was about 10^{15} m^{-3} when the radii of the cathode and the anode were 10 mm and 100 mm, and the cathode voltage was -100 kV . Beam-background reaction rate was almost the same even when the pressure was changed from 1 to 100 mPa since the ion density decreases almost in inverse proportion to the pressure while the neutral density increases in proportion to the pressure. Beam-beam reaction rate increased in inverse proportion to the square of the pressure as the pressure was reduced since the reaction rate is proportional to the square of the ion density. When the cathode voltage was -100 kV , the magnetic field was 200 mT , and the cathode current was 100 mA/m , the estimated fusion reaction rate was $5 \times 10^6 \text{ 1/s/m}$. However, more reaction rate is expected to be achieved since the ion density is expected to become higher when the space charge is neutralized by the electron which is not considered in the present analysis.

References

- [1] R.L. Hirsch, Inertial-electrostatic confinement of ionized fusion gases, *J. Appl. Phys.* 38 (1967) 4522–4534.
- [2] R.F. Radel, G.L. Kulcinski, R.P. Ashley, J.F. Santarius, G.A. Emmert, G.R. Piefer, J.H. Sorebo, D.R. Boris, B. Egle, S.J. Zenobia, E. Alderson, D.C. Donovan, Detection of highly enriched

- uranium using a pulsed D-D fusion source, *Fusion Sci. Technol.* 52 (2007) 1087–1091.
- [3] K. Yoshikawa, K. Masuda, T. Takamatsu, E. Hotta, K. Yamauchi, S. Shiroya, T. Misawa, Y. Takahashi, M. Ohnishi, H. Osawa, Research and development on humanitarian landmine detection system by use of a compact D-D fusion neutron source, *Fusion Sci. Technol.* 52 (2007) 1092–1095.
 - [4] B.B. Cipiti, G.L. Kulcinski, The production of ^{13}N using beam-target D- ^3He fusion reaction, *Fusion Sci. Technol.* 47 (2005) 1245–1249.
 - [5] T. Kobayashi, The status and its future of BNCT irradiation systems using accelerators, in: *Proc. 10th Symposium on Accelerator and Related Technology for Application*, 2008, 12p5.
 - [6] R.F. Radel, PhD. thesis, University of Wisconsin-Madison (2007).
 - [7] K. Yamauchi, S. Ohura, M. Watanabe, A. Okino, T. Kohno, E. Hotta, M. Yuura, Performance of neutron/proton source based on ion-source-assisted cylindrical radially convergent beam fusion, *IEEE Trans. FM* 126 (2006) 1177–1182.
 - [8] M. Ohnishi, H. Osawa, T. Furukawa, T. Suma, Development of convergent D-D fusion neutron generator with large pulse current, *Fusion Sci. Technol.* 52 (2007) 1101–1104.
 - [9] T. Higashi, T. Tomizawa, M. Daino, Y. Yamamoto, Preliminary results of low pressure discharge experiments of a cylindrical inertial electrostatic confinement fusion device aimed for a small neutron source, *Fusion Sci. Technol.* 44 (2003) 544–548.
 - [10] G. Miley, Y. Yang, J. Webber, Y. Shaban, H. Momota, RF ion source-driven IEC design and operation, *Fusion Sci. Technol.* 47 (2005) 1233–1237.
 - [11] G.R. Piefer, J.F. Santarius, R.P. Ashley, G.L. Kulcinski, Design of an ion source for ^3He fusion in a low pressure IEC device, *Fusion Sci. Technol.* 47 (2005) 1255–1259.
 - [12] T. Takamatsu, K. Masuda, T. Kyunai, H. Toku, K. Yoshikawa, Inertial electrostatic fusion device with an ion source using a magnetron discharge, *Nucl. Fusion* 46 (2006) 142–148.
 - [13] K. Yamauchi, K. Ogasawara, M. Watanabe, A. Okino, Y. Sunagawa, and E. Hotta, Neutron production characteristics and emission properties of spherically convergent beam fusion, *Fusion Technol.* 39 (2001) 1182–1187.
 - [14] M. Ohnishi, H. Osawa, R. Tanaka, and N. Wakizaka, Shape of electrodes for high performance of inertial electrostatic confinement fusion, *J. Nucl. Sci. Technol* 42 (2005) 398–405.
 - [15] C.K. Birdsall, Particle-in-cell charged-particle simulations, plus Monte Carlo Collision with neutral atoms, PIC-MCC, *IEEE Trans. Plasma Sci.* 19 (1991) 65–85.
 - [16] IAEA AMDIS ALADDIN database, <http://www-amdis.iaea.org/ALADDIN/>.

- [17] IAEA Evaluated Nuclear Data File, <http://www-nds.iaea.org/exfor/endl.htm>.
- [18] I. Langmuir, K.B. Blodgett, Currents limited by space charge between coaxial cylinders, *Phys. Rev.* 22 (1923) 347–357.

Fig. 1. Definition of the ion current and the potential profile

Fig. 2. Relation between the ion density and the cathode transparency

Fig. 3. Schematic of Magnetic-assisted Electrostatic Confinement device.

Fig. 4. Ideal motion of deuterium molecular ion

Fig. 5. Required magnetic field to avoid colliding with cathode

Fig. 6. Dependence of the ion orbit on the magnetic field

Fig. 7. Lifetime of the ion and the effective cathode transparency vs. background pressure

Fig. 8. Dependence of (a) the ion density distribution and (b) the potential distribution on the background pressure

Fig. 9. Dependence of the energy distribution on the background pressure

Fig. 10. Dependence of the fusion reaction rate on the background pressure

Fig. 11. Dependence of the ion density distribution on the magnetic field

Fig. 12. Dependence of the fusion reaction rate on the magnetic field

Fig. 1

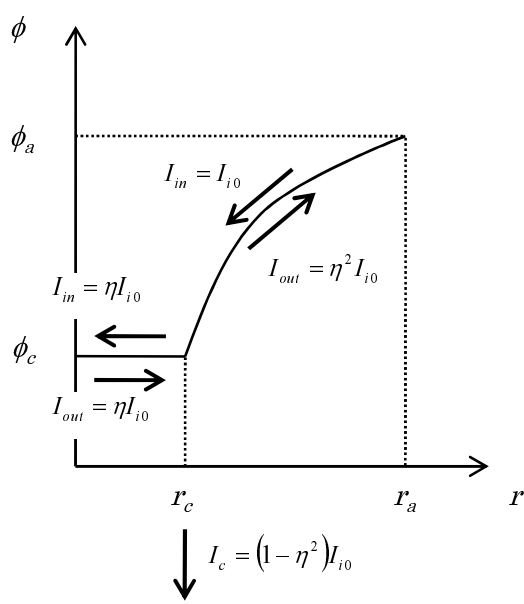


Fig. 2

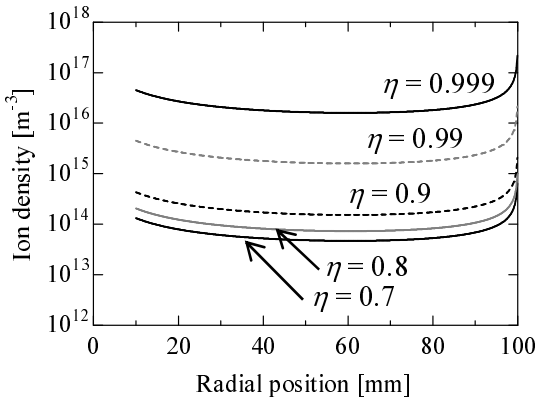


Fig. 3

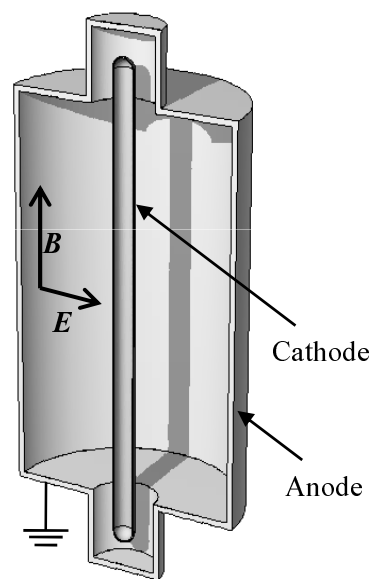


Fig. 4

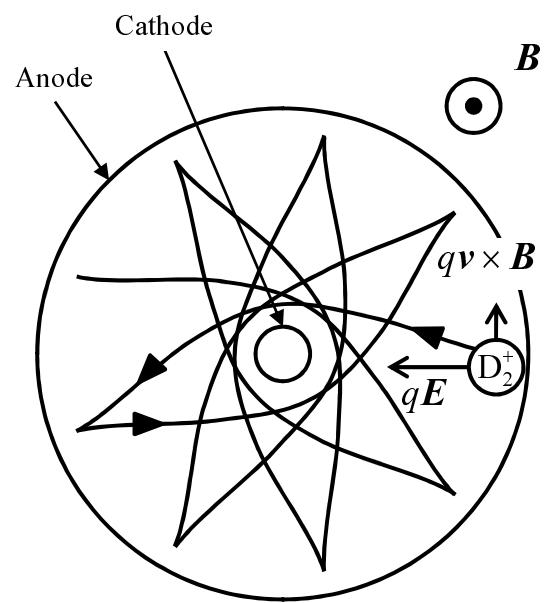


Fig. 5

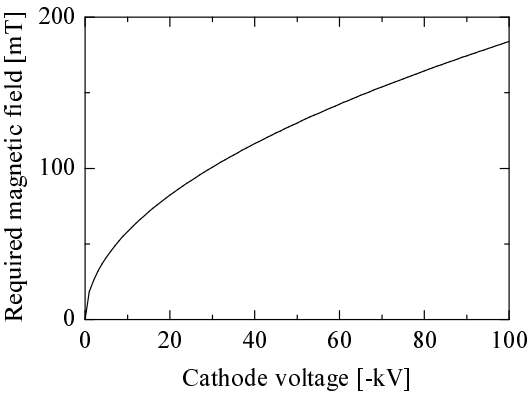


Fig. 6

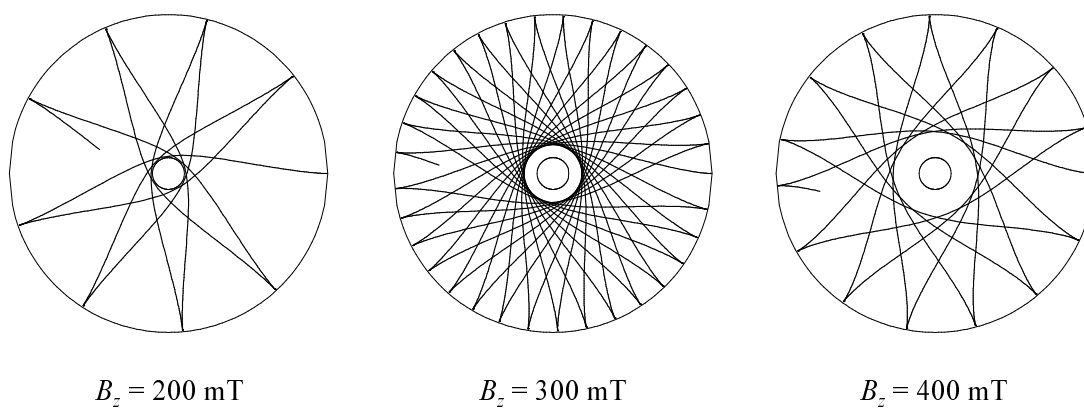


Fig. 7

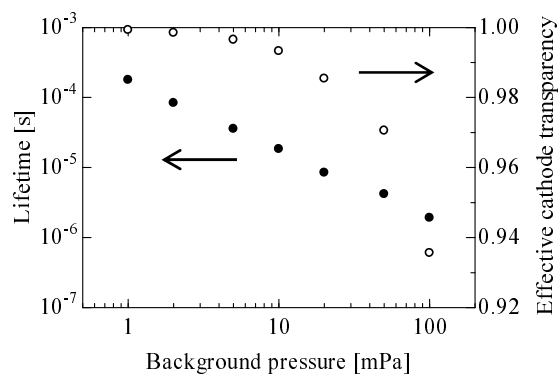


Fig. 8

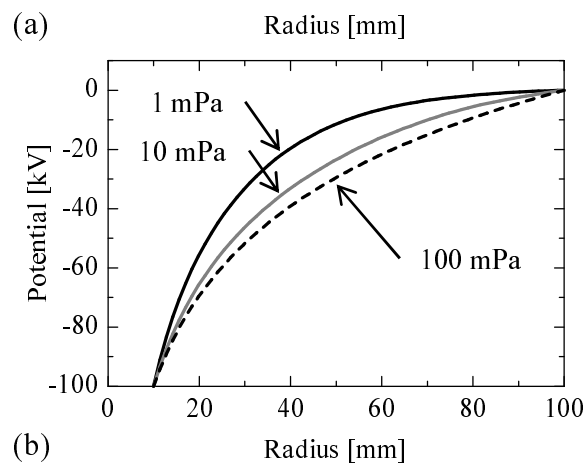
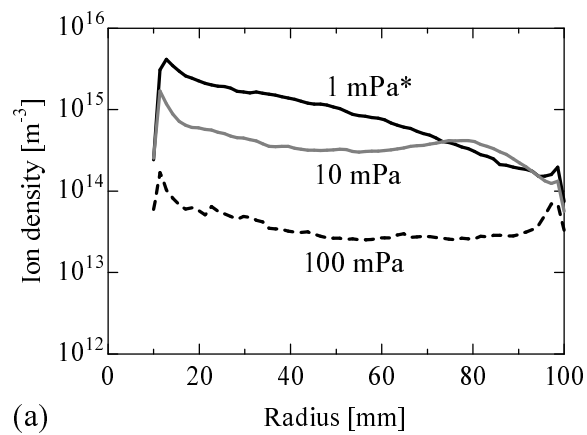


Fig. 9

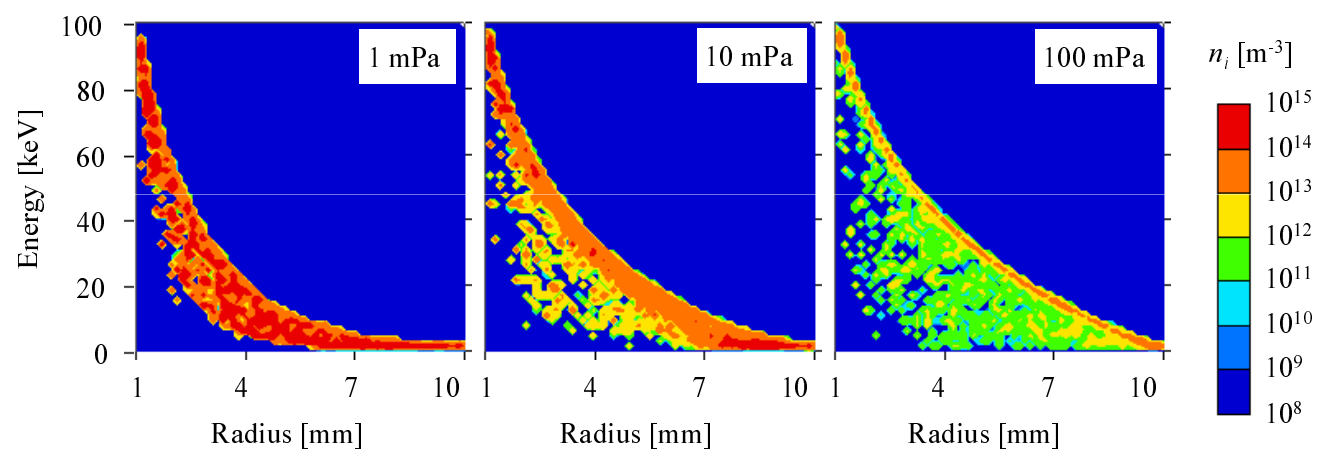


Fig. 9 (black-and-white)

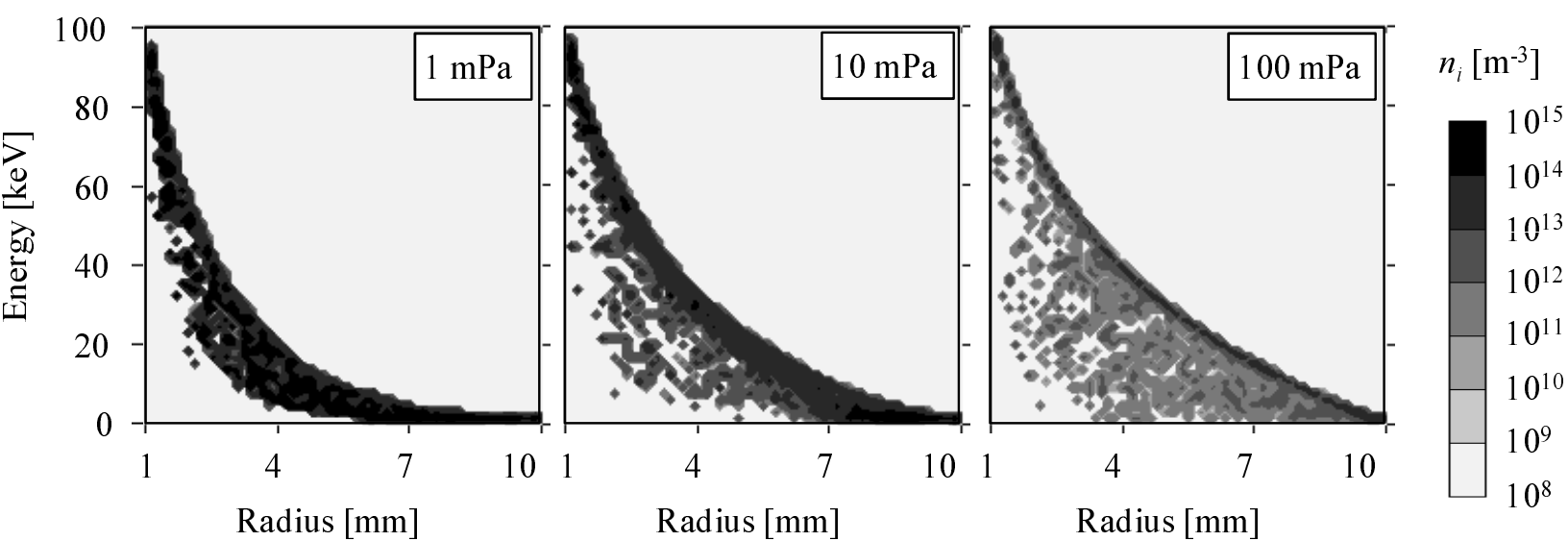

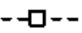






Fig. 10

Cathode current [mA/m]	BM-BG	BM-BM
100		
10		
1		

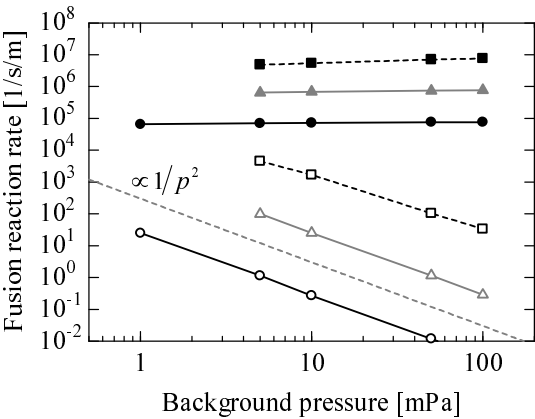


Fig. 11

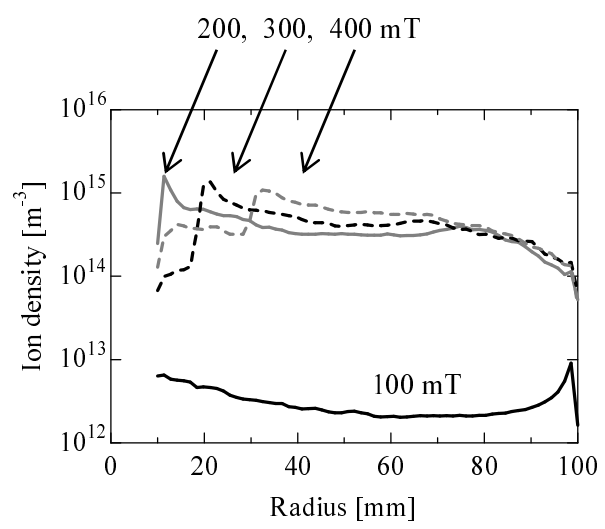


Fig. 12

